THE ASTRONOMICAL JOURNAL, 116:349–359, 1998 July

UNDERSTANDING THE STAR FORMATION PROCESS IN THE FILAMENTARY DARK CLOUD GF 9: NEAR-INFRARED OBSERVATIONS

DAVID R. CIARDI[1] AND CHARLES E. WOODWARD[2]
Wyoming Infrared Observatory, Department of Physics and Astronomy, University of Wyoming, Laramie, WY 82071-3905;
ciardi@hedorah.uwyo.edu, chelsea@kaya.uwyo.edu
DAN P. CLEMENS
Department of Astronomy, Boston University, 725 Commonwealth Avenue, Boston, MA 02215; clemens@protostar.bu.edu
DAVID E. HARKER
Wyoming Infrared Observatory, Department of Physics and Astronomy, University of Wyoming, Laramie, WY 82071-3905;
harker@tana.uwyo.edu
AND
RICHARD J. RUDY
Aerospace Corporation, M2/266, P.O. Box 92957, Los Angeles, CA 90009; rick_rudy@qmail2.aero.org
Received 1998 January 16; revised 1998 March 19

ABSTRACT

We have performed a near-infrared *JHK* survey of a dense core and a diffuse filament region within the filamentary dark cloud GF 9 (LDN 1082). The core region is associated with the *IRAS* point source PSC 20503+6006 and is suspected of being a site of star formation. The diffuse filament region has no associated *IRAS* point sources and is likely quiescent. We find that neither the core nor the filament region appears to contain a Class I or Class II young stellar object. As traced by the dust extinction, the core and filament regions contain 26 and 22 $M_\odot$, respectively, with an average H_2 volume density for both regions of ~ 2500 cm^{-3}. The core region contains a centrally condensed extinction maximum with a peak extinction of $A_V \gtrsim 10$ mag that appears to be associated with the *IRAS* point source. The average H_2 volume density of the extinction core is ~ 8000 cm^{-3}. The dust within the filament, however, shows no sign of a central condensation and is consistent with a uniform-density cylindrical distribution.

Key words: dust, extinction — ISM: clouds — ISM: individual (LDN 1082 = GF 9) — stars: formation

1. INTRODUCTION

Filamentary dark clouds (FDCs), or globular filaments (GFs), are a subclass of small molecular clouds containing somewhat regularly spaced dense cores connected by lower density gas and dust (Schneider & Elmegreen 1979). The filamentary structures of these clouds are most likely affected by the interaction of the cloud material with the ambient Galactic magnetic field, as suggested by optical polarization studies (e.g., McCutcheon et al. 1986). If self-gravity is important in FDCs, the magnetized material is expected to experience gravitational instabilities and fragment into discrete clumps (Chandrasekhar & Fermi 1953). The core masses formed in this way are generally low (tens of solar masses) and expected to gradually contract via ambipolar diffusion to form low-mass stars ($\lesssim 1\ M_\odot$) (Shu, Adams, & Lizano 1987). The relatively slow dissipation of the magnetic field through ambipolar diffusion keeps the core in a subcritical state for a significant time and prohibits the formation of more massive stars (Yang et al. 1991; Shu, Adams, & Lizano 1987).

Previous investigations of FDCs have focused on the star formation properties of individual dense cores within the FDCs (e.g., Benson & Myers 1989; Yang et al. 1991; Goodman et al. 1993). In many cases, these studies have been part of general surveys of low-mass star formation regions and have not represented investigations of an individual FDC (e.g., Myers & Benson 1983; Myers, Linke, & Benson 1983; Beichman et al. 1986; Benson & Myers 1989; Terebey, Vogel, & Myers 1989; Wu, Zhou, & Evans 1992; Goodman et al. 1993). Thus, many individual low-mass star-forming cores associated with FDCs have been studied in relation to other low-mass star-forming cores, but the FDCs, as entities of their own, are relatively unstudied. As a result, little is known about the general star formation properties of FDCs or how the star formation process within the core regions and the filament regions compare.

Many of the cores within FDCs are suspected of being engaged in the process of low-mass star formation (e.g., Beichman et al. 1986), while the filamentary regions are apparently quiescent. FDCs therefore provide a unique environment for a *comparative study* of potential low-mass star-forming and non–star-forming regions within the same host cloud. By studying the structural and kinematic similarities and differences between the distinct environments within an FDC, we can investigate the evolutionary paths of the core and filament regions of FDCs and perhaps gain insight into the evolutionary steps required to transform a non–star-forming region into a star-forming region.

Because of the lower densities associated with the filament regions, only the cold dust within the dense cores of the FDCs appears in the *IRAS* survey. Therefore, we have chosen the core and filament regions for the comparative study based upon the following criteria: (1) the core region must be labeled a "core" in the Schneider & Elmegreen (1979) catalog; (2) the core region must be identifiable in the *IRAS* Sky Survey Atlas; (3) the filament region must be an identifiable structure on the Palomar Observatory Sky Survey plates; and (4) the filament region must not have a

---

[1] NASA Space Grant Fellow.

[2] NSF Presidential Faculty Fellow.

TABLE 1

Comparison of Aerospace Camera and Standard Near-Infrared Filters

Filter	Aerospace Camera (μm) Central λ_0	Aerospace Camera (μm) Half-Power $\Delta\lambda$	Standard Filters[a] (μm) Central λ_0	Standard Filters[a] (μm) Half-Power $\Delta\lambda$
J	1.24	0.26	1.2	0.24
H	1.66	0.30	1.6	0.30
K	2.15	0.32	2.2	0.41

[a] Elias et al. 1982.

corresponding structure visible in the *IRAS* Sky Survey Atlas.

We have undertaken a multiwavelength observational study of two regions within the FDC GF 9 (LDN 1082) to understand how the star formation process within a core region of an FDC compares with that within a filament region. We present our near-infrared results as the first in a series of papers concerning GF 9. The papers to follow include radio isotopic imaging spectroscopy and ISOPHOT far-infrared imaging.

2. OBSERVATIONS

A core and filament region within GF 9 were observed at the broadband near-infrared wavelengths of 1.24, 1.66, and 2.15 μm during the periods 1996 June 6–8 and September 29–30 UT at the 2.34 m Wyoming Infrared Observatory telescope using the Aerospace Corporation near-infrared NICMOS3 HgCdTe camera.

The plate scale of the camera is 0".43 pixel^{-1}, for a total field of view of 110" × 110". The array has a quantum efficiency of $\gtrsim 60\%$ with an approximate dark current of $\lesssim 1$ e^- s^{-1} pixel^{-1}; the readout noise of the electronics is generally $\lesssim 30$ e^- pixel^{-1}. Three cold filters within the dewar were utilized for this project: J, H, and K-short (hereafter referred to as K). J and H are very close to the standard J and H filters (Elias et al. 1982); the K filter is a narrower version of the standard K filter, designed to minimize the long-wavelength thermal background (Rudy, Rossano, & Puetter 1996). We have performed only air-mass extinction corrections to the data, and all magnitudes reported within this paper are in the Aerospace filter system. We estimate that for the reddest sources the K magnitude is underestimated by ~0.1 mag (Wainscoat & Cowie 1992). The characteristics of the Aerospace J, H, and K filters are listed in Table 1.

The core (hereafter GF 9–Core; Fig. 1*a*), listed as GF 9 3C in the Schneider & Elmegreen (1979) catalog, is associated with the *IRAS* point source PSC 20503+6006 and is suspected of being engaged in star formation (e.g., Myers, Linke, & Benson 1983; Beichman et al. 1986; Benson & Myers 1989; Bontemps et al. 1996; Saraceno et al. 1996). The 12, 25, 60, and 100 μm *IRAS* fluxes of PSC 20503+6006 are <0.05, 0.37, 1.5, and <14.0 Jy, respectively (Beichman et al. 1986) with a corresponding *IRAS* spectral index of $\alpha = -1.5$, indicating that the PSC 20503+6006 is likely a Class I or younger protostar (Beichman et al. 1986; Ciardi 1997). The diffuse filament region (hereafter GF 9–Fila; Fig. 1*b*) has no *IRAS* point sources associated with it and likely is quiescent. The central map positions for the core and filament regions observed in this work are listed in Table 2.

GF 9–Core and GF 9–Fila were imaged using a 5 × 5 equatorially oriented mosaic map. Each array placement overlapped the previous array placement by ~27" (one-fourth of the array), providing a total sky coverage of 7' × 7'. To ensure proper pointing and tracking, the central map position was observed at the beginning, middle, and end of each raster map. The relative positions of the sources in the central frames agree to within ~1" from the beginning to the end of the mosaic maps. Note that because of an initial pointing error, the center of the GF 9–Core mosaic taken on 1996 June 8 is actually located at $\Delta\alpha = 0'.5$, $\Delta\delta = -0'.5$ with respect to the coordinates listed in Table 2. For consistency with the papers to follow, all offsets are listed with respect to the nominal positions listed in the table.

The survey observations were obtained at an air mass of $X \lesssim 1.15$ with an integration time of 9.5 s per frame. Near-infrared standard stars were chosen from the faint-standard list of Elias et al. (1982). During 1996 September 29–30 UT, additional J, H, and K images of four lines of sight ~30' north of GF 9–Fila were obtained, with each field separated by 200" from each neighboring field. Along these lines of sight, the sky is apparently devoid of extinction or molecular emission, and therefore, we used measurements of stars in these fields to "calibrate" the near-infrared colors of sources background to GF 9.

Finally, the regions of highest extinction in GF 9–Core and GF 9–Fila were observed at an integration time of 40 s. The longer integrations were performed to enhance the extinction measurements and to search for deeply embedded sources that may not have been detected at an adequate signal-to-noise ratio above the background in the survey images. All observations are summarized in Table 3.

Point sources in the final images were extracted using an IDL version of DAOFIND (Stetson 1987) with a search FWHM aperture of 3 pixels and a threshold level of 4 times the rms sky noise. Aperture photometry was performed using an IDL version of the IRAF[3] routine APPHOT on those sources found with DAOFIND. The aperture radii were set to the optimal value of r = FWHM of the point-spread function (Howell 1989). Setting the aperture size to the FWHM may undersample the stellar profiles, and thus, the derived fluxes are likely to be lower limits. However, the derived *color indexes* should be unaffected by the choice of aperture, as the point-spread functions for all three filters for a variety of sources were compared and were found to agree within a few percent.

Sources found in the three filters were cross-referenced by position to produce a list of *JHK* sources. All sources with a

---

[3] IRAF is distributed by the National Optical Observatories, which are operated by the Association of Universities for Research in Astronomy, Inc., under cooperative agreement with the National Science Foundation.

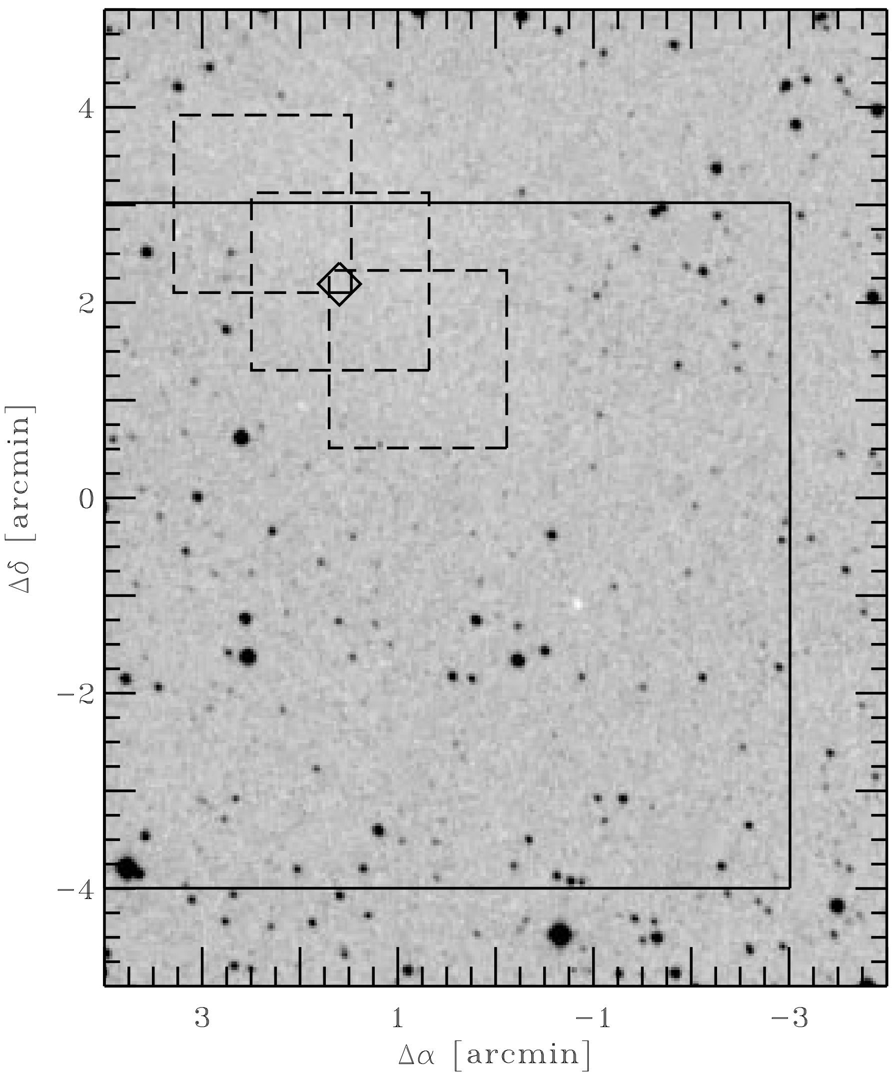

FIG. 1*a*

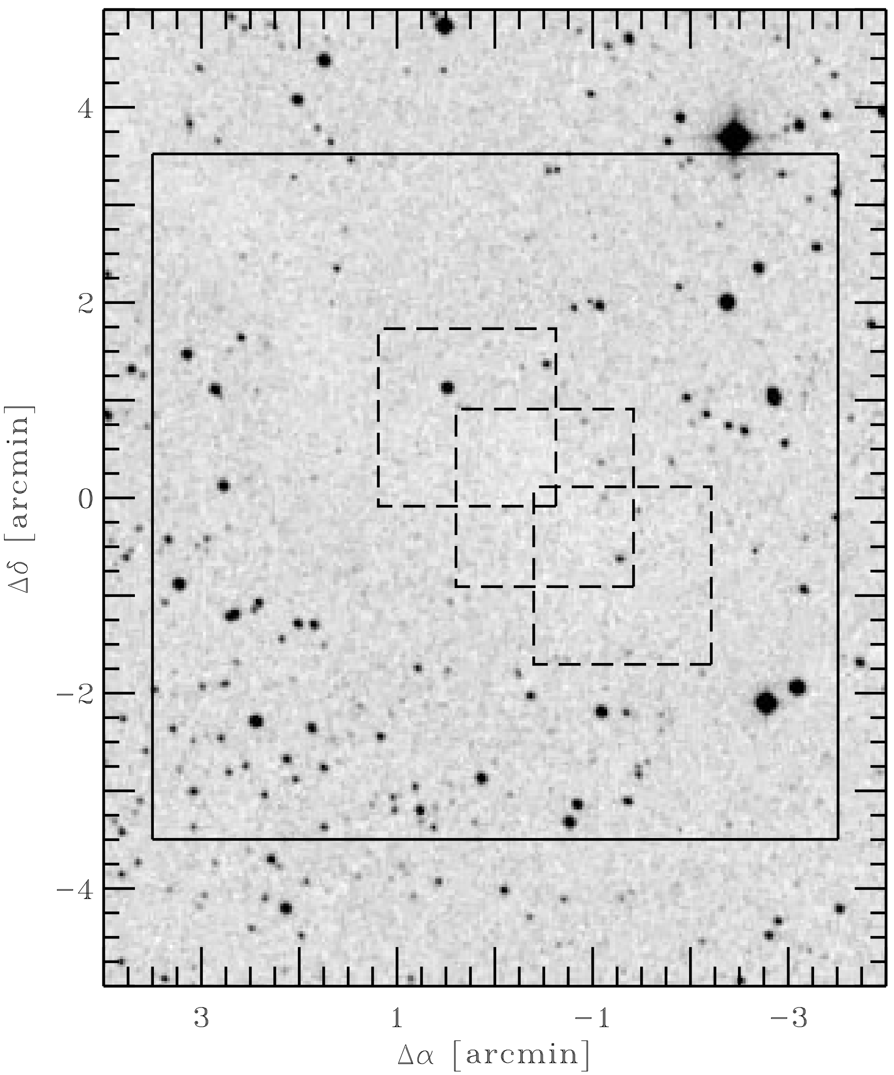

FIG. 1*b*

FIG. 1.—Optical image of (*a*) GF 9–Core and (*b*) GF 9–Fila from the Digitized Sky Survey. The images are $10' \times 8'$ and are centered on the positions listed in Table 2. In (*a*), the diamond at $\Delta\alpha = 1\farcm6$, $\Delta\delta = 2\farcm17$ marks the position of the *IRAS* point source PSC 20503+6006. The large square delineates the region of the near-infrared survey, and the dashed squares delineate the regions of the deep integrations.

TABLE 2

CENTRAL COORDINATES OF REGIONS OBSERVED WITHIN GF 9

Region	α (B1950.0)	δ (B1950.0)
GF 9–Core……	20 50 07	60 04 31
GF 9–Fila…….	20 48 02	60 00 27

NOTE.—Units of right ascension are hours, minutes, and seconds, and units of declination are degrees, arcminutes, and arcseconds.

signal-to-noise ratio of less than 3 in any filter were rejected from the sample. The average number of *JHK* sources found per frame was ~16, for a total source count of 395 toward GF 9–Core and 361 toward GF 9–Fila. Approximately 25% of the sources were imaged in more than one mosaic frame. The approximate 80% completeness limits of this survey were 16.5, 15.5, and 15.4 mag for *J*, *H*, and *K*, respectively. We estimate that for the pointed 40 s observations the completeness limits were extended by ~1.5 mag within each filter.

In Figures 2*a* and 2*b*, the positions of all sources detected toward GF 9–Core and GF 9–Fila are plotted. The absolute positional error was estimated from sources that have optical counterparts in the Digitized Sky Survey[4] and was found to be ~10″ or less. A 10′ × 8′ area is displayed for comparison with new molecular maps of the GF 9 region (Ciardi et al. 1998).

TABLE 3

SUMMARY OF OBSERVATIONS

Parameter	GF 9–Core	GF 9–Fila[a]	Control
Observation date (UT)……	1996 Jun 8	1996 Jun 7	1996 Sep 29
Map mode ………………	5 × 5 mosaic	5 × 5 mosaic	Four pointed positions
Filters……………………	*JHK*	*JHK*	*JHK*
Frame $T_{\rm int}$ (s) ……………	9.5	9.5	9.5
($\Delta\alpha$, $\Delta\delta$) (arcmin):[b]			
Position 1 …………….	1.6, 2.2	−0.5, 0.0	…
Position 2 …………….	2.4, 3.0	0.3, 0.8	…
Position 3 …………….	0.8, 1.4	−1.3, −0.8	…

[a] Three of the fields were observed on 1996 June 8.

[b] Central positions of deep frames (40 s) taken in 1996 September.

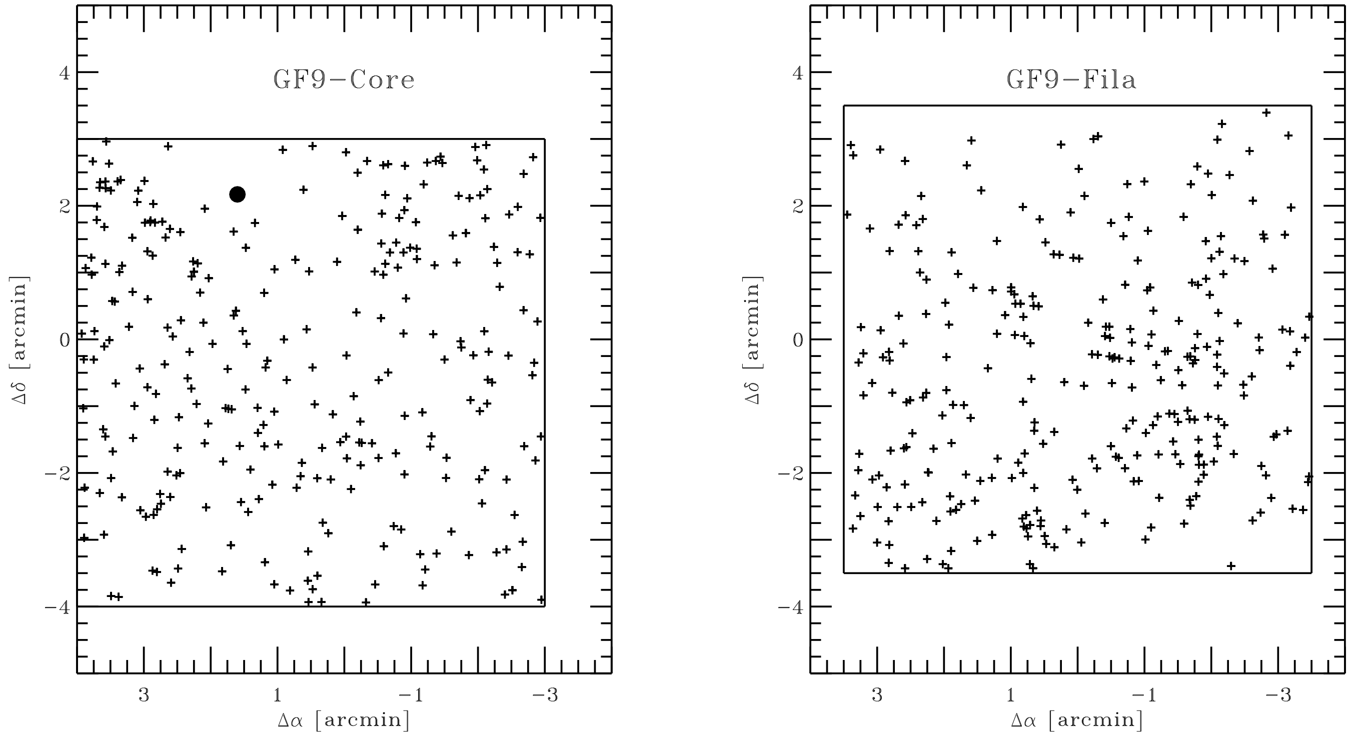

FIG. 2*a*

FIG. 2*b*

FIG. 2.—All positions of the detected near-infrared sources for (*a*) GF 9–Core and (*b*) GF 9–Fila. The entire plot encompasses 10′ × 8′ corresponding to the region mapped in CO and CS (Ciardi et al. 1998). The large square delineates the region for the near-infrared survey. The circle in (*a*) represents the position of the *IRAS* point source PSC 20503+6006 ($\Delta\alpha = 1'.6$, $\Delta\delta = 2'.17$).

---

[4] Based on photographic data of the National Geographic Society–Palomar Observatory Sky Survey (POSS-I) obtained using the Oschin Schmidt telescope on Palomar Mountain. The POSS-I was funded by a grant from the National Geographic Society to the California Institute of Technology. The plates were processed into the present compressed digital form with their permission. The Digitized Sky Survey was produced at the Space Telescope Science Institute under US government grant NAGW-2166.

3. DISCUSSION

3.1. *Search for Embedded Near-Infrared Sources*

Near-infrared *JHK* color-color plots are a powerful diagnostic tool for investigating the nature of stellar objects, including Class I and Class II young stellar objects (YSOs) (Lada & Adams 1992). Class I and Class II YSOs are expected to have large positive infrared colors ($J-H \gtrsim 2$, $H-K \gtrsim 1$) and should be identifiable on a color-color diagram by their infrared excess caused by the presence of circumstellar dust (Yun & Clemens 1995). Class I and Class II YSOs should, therefore, separate themselves from normally reddened main-sequence stars in a *JHK* color-color diagram (Lada & Adams 1992). In Figure 3, the near-infrared color-color diagrams for GF 9–Core and GF 9–Fila are presented.

In a study by Yun & Clemens (1995), 22 suspected protostars detected by their *IRAS* colors (Yun & Clemens 1990) were observed in the near-infrared *J*, *H*, and *K* filters. The near-infrared counterparts to the *IRAS* points sources were identified and classified as either Class I or Class II YSOs. The *faintest* near-infrared counterpart had a *K* magnitude of ~13.9 mag. At a minimum distance of 100 pc (Kane 1995), a source with an apparent magnitude of $K = 13.9$ mag ($M_K = 8.9$ mag) would have an apparent magnitude of $K \sim 16$ mag at the distance of GF 9 (440 pc; Dobashi et al. 1994). A $K = 16$ mag source falls just beyond our conservative estimates of the completeness limits, but could possibly be detected within the limit of our signal-to-noise ratio. Our data should be deep enough to detect a Class I or Class II YSO at the distance of GF 9. However, younger Class 0 protostars and pre–protostellar cores are undetectable from the ground at wavelengths shorter than about 10 μm (Barsony 1994).

3.1.1. *GF 9–Core*

As discussed in § 1, the *IRAS* point source PSC 20503+6006 is a suspected protostar and, therefore, may be associated with a near-infrared point source if it is a Class I or Class II YSO. The positional error on the *IRAS* point source PSC 20503+6006 is described by an error ellipse with a semimajor axis of 18″, semiminor axis of 6″, and a position angle of 31° east of north (*IRAS* Explanatory Supplement 1988). The one GF 9–Core source in Figure 3 that exhibits an apparent infrared color excess (i.e., to the right of the stellar reddening zone) is not spatially coincident with the *IRAS* point source. At near-infrared wavelengths, it is ~2′ west of PSC 20503+6006, effectively ruling out this source as a near-infrared counterpart.

Three sources were found to be within a 0′.75 radius of the PSC position, and of these three, the reddest source ($J-H = 1.74$, $H-K = 0.72$) also is the source closest ($\Delta\alpha = -1'.34$, $\Delta\delta = 1'.74$) to the *IRAS* point source PSC 20503+6006. However, it should be noted that we detected no sources directly to the north of the *IRAS* point source, which indicates that the highest extinction region lies to the north of PSC 20503+6006. In addition, we have found from ^{13}CO and CS observations that the densest gas also lies to the north of the *IRAS* point source (Ciardi 1997; Ciardi et al. 1998). Thus, the near-infrared source detected

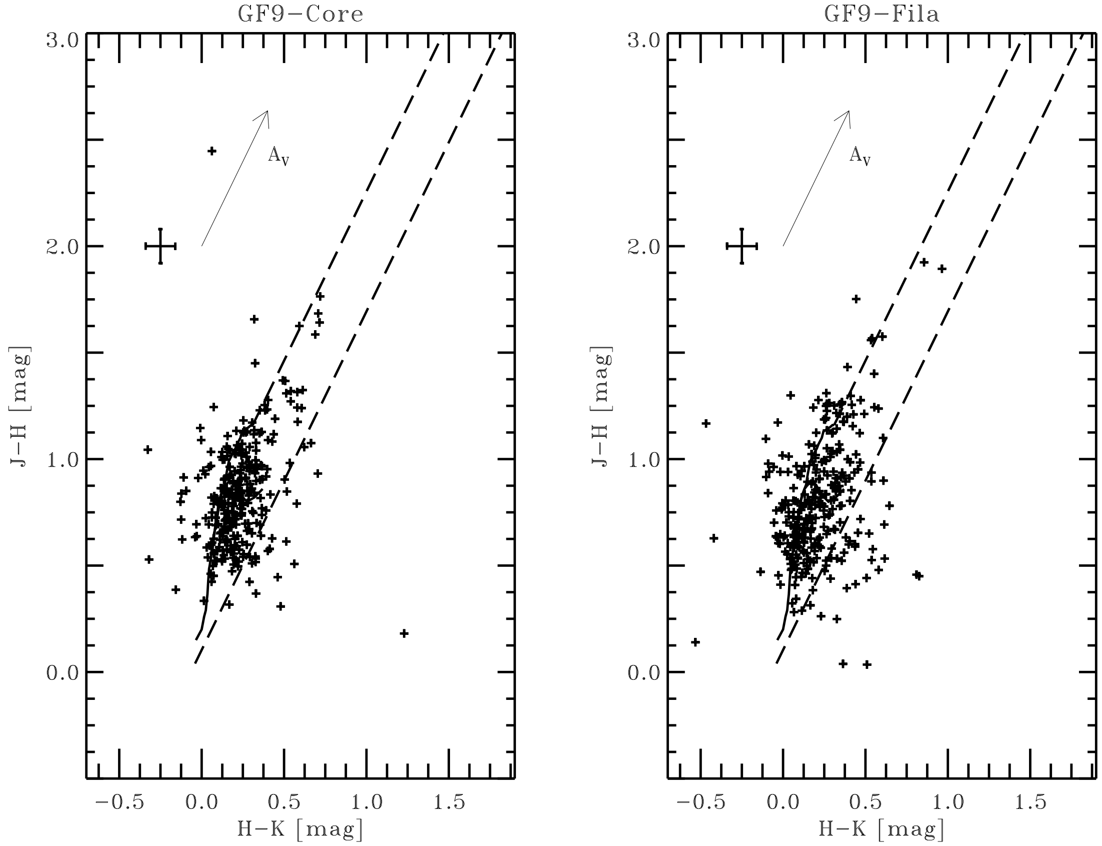

FIG. 3.—*JHK* color-color diagram for GF 9–Core (*left*) and GF 9–Fila (*right*). The dashed lines represent the boundaries for the reddening zone. The unreddened main sequence and giant branch are represented by solid lines. The arrow represents the direction and reddening for $A_V = 5$ mag. Typical 1 σ error bars are shown in the upper left of each plot.

closest to PSC 20503+6006 most likely is a heavily reddened background star that happens to lie near the same line of sight as does PSC 20503+6006. We conclude that GF 9–Core does not contain a Class I or II YSO brighter than $K \sim 16$ mag. If PSC 20503+6006 possesses a near-infrared counterpart, it is either heavily obscured, of low luminosity ($M_K > 8$ mag), or both.

3.1.2. *GF 9–Fila*

In GF 9–Fila, four sources were identified by a large $H-K$ color index ($\gtrsim 0.7$ mag). Of these four, two were located within $\lesssim 1'$ of the central region of the filament. However, both sources displayed colors consistent with heavily extinguished stars ($J-H \sim 1.9$, $H-K \sim 0.9$). The other two sources are located in Figure 3 well to the right of the "normal reddening" zone. However, the sources are quite faint ($K \sim 16$ mag), and the errors associated with the near-infrared colors are large ($\sigma_{H-K} \gtrsim 0.25$ mag). Both sources also are located near the periphery ($\gtrsim 2'$ from map center) of the cloud where the extinction $A_V \lesssim 1.5$ mag (see § 3.3). Our ^{13}CO and CS observations reveal that no significant dense gas is spatially coincident with these sources (Ciardi 1997; Ciardi et al. 1998). Thus, it is unlikely that these two sources are embedded YSOs.

3.2. *Color Excess and Extinction Maps*

3.2.1. *Color Calibration with the Control Fields*

The wavelength dependence of the dust extinction properties causes starlight to exhibit a reddening, or color index excess, defined as

$$E(H-K) = (H-K)_{\text{observed}} - (H-K)_{\text{intrinsic}} , \quad (1)$$

which is directly proportional to the line-of-sight dust column density (e.g., Lada et al. 1994). We have estimated the average intrinsic color index through analysis of the control-field observations. By assuming that the stars within the control fields are representative of the stars behind the molecular cloud and that the stars do not suffer significant extinction, we have used the average near-infrared colors of the control-field stars to estimate the intrinsic color index of the stars background to the cloud (e.g., Lada et al. 1994).

The error-weighted mean $H-K$ color index of the control-field sources was measured to be

$$(H-K)_{\text{intrinsic}} \equiv \langle (H-K) \rangle_{\text{control}} = 0.09 \pm 0.03 \text{ mag} . \quad (2)$$

In addition, the error-weighted mean $J-H$ intrinsic color index was 0.49 ± 0.03 mag. The mean $J-H$ and $H-K$ color indexes correspond to the color indexes of an early K-type main-sequence star (K2) or a late G-type giant star (G8), both of which agree with the expected stellar population distribution toward this line of sight ($l \sim 97°$, $b \sim 10°$) (Bessel & Brett 1988; Garwood & Jones 1987).

3.2.2. *Extinction Maps*

Using the mean color indexes for the control-field sources, the $H-K$ color excess was calculated for each of the 700-plus sources detected toward GF 9–Core and GF 9–Fila. From the database of positions and $H-K$ color excesses, information about the distribution of extinction through the cloud can be determined at a very high spatial resolution ($1''$–$2''$). However, the map of extinction through the cloud at this resolution is highly undersampled and nonuniform. By spatially smoothing, we constructed a uniform and well-sampled map of the distribution of extinction through GF 9. Each sample box was $50'' \times 50''$ and was separated from neighboring sample boxes by $25''$, yielding a Nyquist-sampled moderate-resolution extinction map of the cloud (e.g., Lada et al. 1994).

In determining the mean color excess of all the stars falling within a bin, those stars that showed a negative $E(H-K)$ were considered foreground stars and culled from the database. Toward GF 9–Core, 20% of the sources were found to possess negative $E(H-K)$ while, toward GF 9–Fila, 25% of the sources had negative $E(H-K)$. The remaining stars were binned and an error-weighted mean $E(H-K)$ was determined for each bin. Because the color excess is proportional to the line-of-sight column density of the dust, the fully sampled color excess map is equivalent to a fully sampled dust column density map. However, if the cloud is significantly clumpy on angular scales smaller than the sample size, then the sample area may be preferentially skewed toward less extinguished stars shining through the lower density regions (Frerking, Langer, & Wilson 1982). Thus, the extinction measured toward each line of sight is likely a lower limit to the true extinction, and the calculated masses and densities will also be lower limits.

It is convenient to represent the dust column density map in terms of the visual extinction, A_V (e.g., Bok 1937; Greenstein 1951; Straw & Hyland 1989; Lada et al. 1994). To do so we must apply the ratio of total to selective extinction [$R \equiv A_V/E(B-V)$] for the dust in the molecular cloud. The value of R can vary greatly depending upon the interstellar medium environment along the line of sight; values as low as $R = 2.75$ to as high as $R = 5.3$ have been observed (e.g., Mathis 1990). In general, lower density regions display values of $R \sim 3$ and higher density regions display values of $R \sim 5$. However, it is not always possible to estimate R from the environmental conditions. For example, values of ~ 3.0–3.5 have been measured in parts of the dense Taurus molecular cloud complex (Vrba & Rydgren 1985).

The variation of the near-infrared ($\lambda \gtrsim 1$ μm) extinction toward different lines of sight is quite small for wide a range of R-values (Cardelli, Clayton, & Mathis 1989). Therefore, we cannot determine the local value of R for GF 9 with the current data. For simplicity and ease of comparison with other works (e.g., Dickman & Herbst 1990), we have chosen to use the "standard" interstellar medium value of $R = 3.1$ (e.g., Rieke & Lebofsky 1985). The mean color excess at each point in the map can be converted to an equivalent mean visual extinction via $\langle A_V \rangle = 15.9 \langle E(H-K) \rangle$. If instead we assume that $R = 5$, the visual extinction calculated from the infrared color excesses would be $\sim 20\%$ lower.

Finally, four of the $50''$ boxes toward GF 9–Core contained no sources, because of the large line-of-sight extinction toward the position of PSC 20503+6006. The $E(H-K)$ for these pixels were set to the highest mean color excess calculated for the Nyquist-sampled map [$E(H-K) = 0.63$ mag; $A_V \sim 10$ mag]. Clearly, this is only a lower limit estimate of the true extinction toward that line of sight. The visual extinction maps generated under the assumptions outlined above are presented in Figures 4*a* and 4*b*.

Presented in Figure 5 are histograms of the visual extinction measured toward GF 9–Core and GF 9–Fila. For the core region, the average extinction is $A_V \sim 3$ mag with a

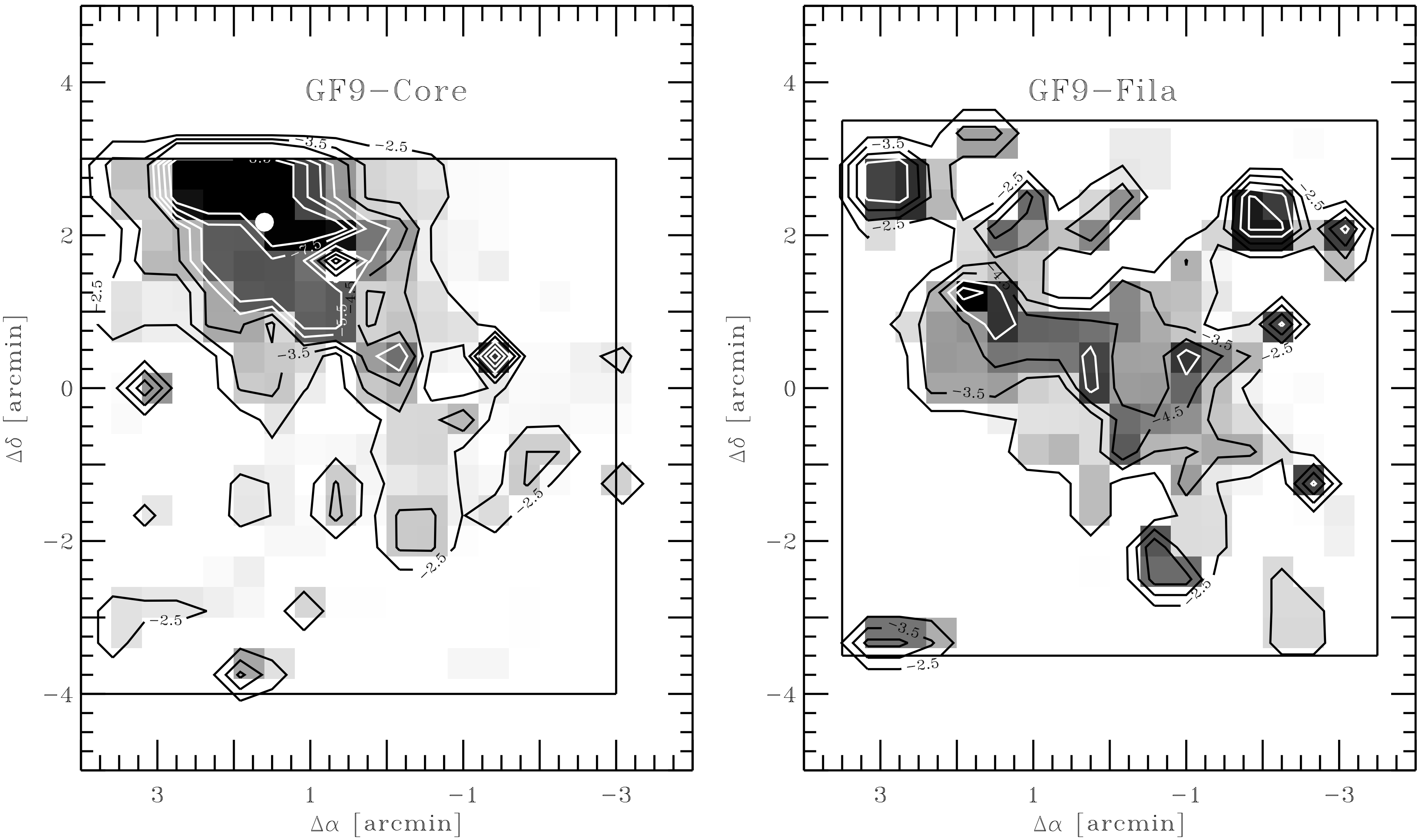

FIG. 4*a*

FIG. 4*b*

FIG. 4.—(*a*, *b*) Maps of the mean visual extinction toward GF 9–Core and GF 9–Fila derived from the $H-K$ color excess of the sources plotted in Figs. 2*a* and 2*b*, respectively. The contours start at $A_V = 2.5$ mag and are stepped by 1.0 mag. The large square delineates the region for the near-infrared survey. The small white circle in (*a*) represents the position of the *IRAS* point source PSC 20503 + 6006 ($\Delta\alpha = 1'.6$, $\Delta\delta = 2'.17$).

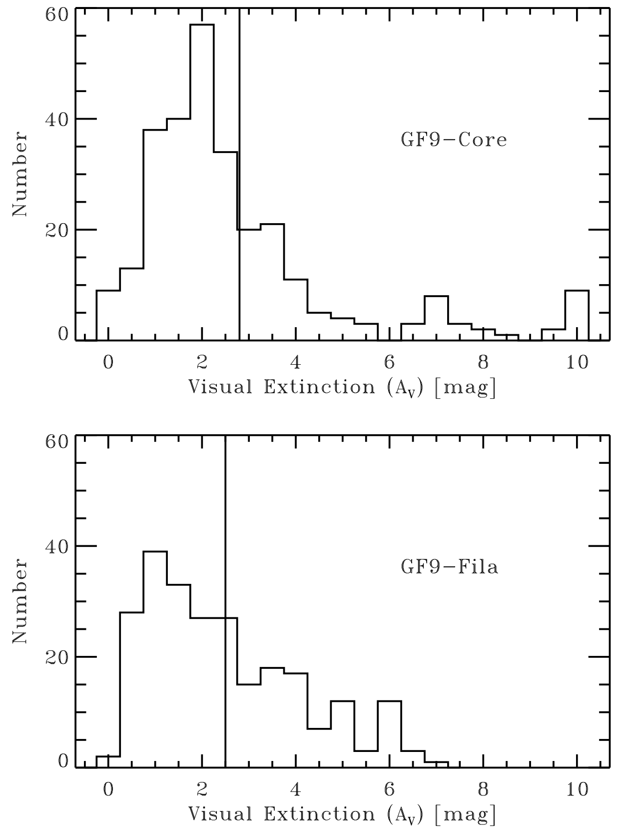

FIG. 5.—Histograms of the visual extinction measured toward GF 9–Core (*top*) and GF 9–Fila (*bottom*). The vertical lines represent the mean extinction values measured toward each region: 2.8 mag and 2.5 mag, respectively.

maximum value of $A_V \sim 10$ mag. The apparent excess at $A_V = 10$ mag is a result of setting the empty pixels in the high-extinction region to the maximum value measured. We have *not* sampled the complete range of extinction present toward GF 9–Core.

For GF 9–Fila, it is evident that (to the resolution of the Nyquist map), we have sampled the complete range of extinction present. The average extinction is $A_V \sim 2.5$ mag, but the maximum value is only $A_V \sim 7$ mag, a full 3 mag below the maximum found toward GF 9–Core. It is noteworthy that the distribution of pixels below an extinction of $A_V \sim 5$ mag is quite similar to the distribution seen toward GF 9–Core. It is only when the extinction rises above $A_V = 5$ mag that the two distributions begin to differ.

3.3. *Mass and Density Structure*

The observed gas-to-dust ratio in interstellar clouds has been found to be relatively constant (e.g., Lilley 1955; Jenkins & Savage 1974; Bohlin, Savage, & Drake 1978; Frerking, Langer, & Wilson 1982; Lada et al. 1994). As the extinction (A_λ) is directly proportional to the column density of the dust, the measured extinction can be used to calculate the column density of the gas, assuming a constant gas-to-dust ratio. Bohlin, Savage, & Drake (1978) measured a ratio of gas column density to color excess of

$$\left\langle \frac{N(\mathrm{H\,I}) + 2N(\mathrm{H_2})}{E(B-V)} \right\rangle = 5.8 \times 10^{21}\ \mathrm{atoms\ cm^{-2}\ mag^{-1}}\ . \tag{3}$$

If we assume that $R = 3.1$ and that the hydrogen gas is in molecular form (Frerking, Langer, & Wilson 1982), then we arrive at a ratio of gas column density to visual extinction of

$$\left\langle \frac{N(\mathrm{H_2})}{A_V} \right\rangle = 0.94 \times 10^{21}\ \mathrm{molecules\ cm^{-2}\ mag^{-1}}\ . \tag{4}$$

The transformation relation given by equation (4) was used to generate molecular hydrogen (H_2) column density maps from our observed extinction maps (Fig. 4). Note that $E(H-K)$ is relatively insensitive to extinction of $A_V \lesssim 2$ mag, and therefore, if lower density gas fills a large area, then the extinction measurements may underestimate the total mass by a significant amount. Thus, the masses calculated from the color excesses represent lower limits to the true cloud mass.

3.3.1. *GF 9–Core*

Converting visual extinction into hydrogen column density via equation (4), we find that the average column density is $\sim 2 \times 10^{21}$ cm^{-2} with a peak column density of $\sim 10 \times 10^{21}$ cm^{-2}. With an assumed distance of 440 pc (Dobashi et al. 1994), we calculate for GF 9–Core a total mass of $\sim 26\ M_\odot$ for $A_V \gtrsim 2.5$ mag. Below an extinction of $A_V \sim 2.5$ mag, the measured color excesses $E(H-K) \lesssim 0.15$ mag are less than 3 σ and are considered relatively unreliable.

Based upon the extinction map displayed in Figure 4*a*, we estimate that GF 9–Core spans $6' \times 4'$ at a position angle of $\sim 45°$ east of north. Assuming that GF 9–Core can be approximated with a three-dimensional ellipsoid ($6' \times 4' \times 4'$), we obtain an average density of $\langle n \rangle = 2800$ cm^{-3}. Note that the mean density calculated is likely a lower limit, as the data do not fully sample the region nor have we accounted for the fragmentation of the cloud.

The most significant density concentration occurs at the location of the *IRAS* point source PSC 20503+6006: $\Delta\alpha \sim 2'$, $\Delta\delta \sim 2\overset{'}{.}5$. In Table 4, the mass and density properties of GF 9–Core (as a whole) and the region surrounding the suspected protostar (PSC 20503+6006) are compared. The size of the high-extinction core was estimated from the FWHM ($1\overset{'}{.}3$) of the column density distribution (Fig. 6). The region near the *IRAS* point source was found to

TABLE 4

MASS AND DENSITY FOR GF 9

	GF 9–CORE		GF 9–FILA	
PARAMETER	Average	High-Extinction Region	Average	Central Extinction Region
Total mass ($M_\odot$)......	26	9.3	22	15
Radius (pc)	0.38 × 0.26	0.17	0.45 × 0.38	0.28
$\langle n \rangle$ (cm^{-3})	2800	8000	2300	2800
n_{peak} (cm^{-3})	...	9100	...	3900

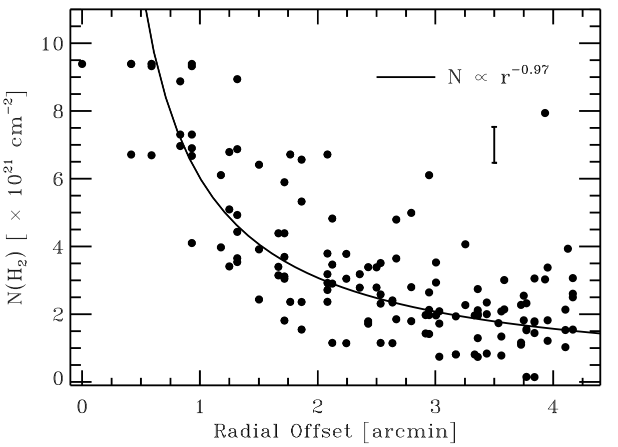

FIG. 6.—GF 9–Core radial hydrogen column density profile centered at $\Delta\alpha = 2'$, $\Delta\delta = 2'.5$. The solid line represents the best-fit power law ($\alpha = -0.97 \pm 0.24$) to the data and was fitted to the data outside $r \gtrsim 0'.75$. A typical 1 σ error bar is shown near the center of the plot.

contain 9.3 $M_{\odot}$, almost 35% of the total mass in GF 9–Core. In addition, the density of the region near the *IRAS* point source is significantly higher (~3 times) than the density for the cloud as a whole.

A power law of the form $n(r) \propto r^{\gamma}$ is usually used to describe the radial volume density profile inside a molecular cloud (e.g., Yun & Clemens 1991). In order to relate the observed radial column density profile $[N(r) \propto r^{\alpha}]$ to a radial volume density profile, we have applied the method of Yun & Clemens (1991), where $\gamma = \alpha + 1 + \Delta\gamma$. The correction value $\Delta\gamma$ is dependent upon the fractional radius of the cloud sampled by the data. Because of the long extended shape of GF 9 as a whole, estimating the fractional radius is somewhat difficult. If the near-infrared survey covers the majority of the region, then the fractional radius is 1; however, it is clear from the extinction map that GF 9–Core extends to the north beyond the limit of the near-infrared survey. We therefore have estimated the correction factors for a range of fractional radii of 0.5–1.0.

In Figure 6, the H_2 column density of GF 9–Core as a function of radius is shown. The reference point for the radial offsets is $\Delta\alpha = 2'$, $\Delta\delta = 2'.5$. As a result of the undersampling of the high-extinction region, the linear least-squares fit to the H_2 column density profile was performed on the data outside the region of saturation ($r \gtrsim 0'.75$). The best-fit power-law profile for the column density distribution was calculated to be $N(r) \propto r^{-0.97\pm0.24}$. For the range of expected fractional radii, we estimate the γ-correction factor to be $\Delta\gamma = -0.4 \pm 0.2$ (Yun & Clemens 1991), yielding a volume density profile of the form $n(r) \propto r^{-1.57\pm0.31}$, a value indistinguishable from what is expected from free-fall collapse models ($\gamma = -3/2$; Shu 1977). Clearly, GF 9–Core is centrally condensed at the position of the *IRAS* point source.

3.3.2. *GF 9–Fila*

Converting the visual extinction in GF 9–Fila to H_2 column density, we find (for $A_V \geq 2.5$ mag) a total mass of ~22 $M_{\odot}$, which is ~15% less than what was measured for GF 9–Core. GF 9–Fila is elongated at a position angle of ~45° east of north with a semimajor axis of ~$3'.5$ and a semiminor axis of ~$3'$ (Fig. 4*b*). Assuming an ellipsoidal volume, the average volume density for GF 9–Fila was found to be $\langle n \rangle \sim 2300\ cm^{-3}$, a value very near the average density calculated for GF 9–Core.

From Figure 4*b*, it is evident that there are no high-extinction cores ($A_V \gtrsim 5$ mag) in GF 9–Fila as there appears to be in GF 9–Core. However, if the H_2 column density is plotted as a function of radial distance from map center ($\Delta\alpha = 0'$, $\Delta\delta = 0'$), a scattered but somewhat smooth decline can be seen (Fig. 7). The binned averaged radial profile in Figure 7 (*filled circles*) displays a plateau region of $N = 3.3 \times 10^{21}\ cm^{-2}$ for $r \lesssim 1'$ and a power-law decline for $r \gtrsim 1'$ of the form $N(r) \propto r^{-0.60\pm0.25}$.

As discussed above, it is clear that GF 9–Fila does not contain a strong central condensation as is contained in GF 9–Core. In fact, the distribution of the dust within GF 9–Fila appears to be fairly uniformly distributed (Fig. 4*b*). Thus, it is possible that the radial decline of the column density profile is simply a result of viewing the edges of the cloud. To test this hypothesis, we have modeled a uniform volume density cylindrical cloud with a maximum visual extinction of $A_V = 3.6$ mag and a background extinction level of $A_V = 1.8$ mag. The radius of the cylindrical model was $r = 3'$ and the length was $l = 7'$. Finally, the cylinder was assumed to be viewed face-on.

In Figure 8, the radially averaged data from Figure 7 (*filled circles*) are compared with the model radial profile (*solid line*). In excellent agreement with the data, the model is found to have a plateau region for $r \lesssim 1'$ and a power-law decline for $r \gtrsim 1'$. The model power law is characterized by $\alpha = -0.63$, which agrees with the measured value of -0.60 ± 0.25. Although in reality we would expect the volume density to decline near the cloud edges, the model shows that a uniform-density cylindrical cloud is a reasonable facsimile of the actual structure of GF 9–Fila.

As a final test of the uniform-cylinder model, the radius of the central region in GF 9–Fila was estimated to be $2'.2$ from the FWHM in Figure 7. The mass contained within this radius is ~15 $M_{\odot}$, which is ~65% of the total mass measured for GF 9–Fila. The mean volume density of region within $2'.2$ of the center was measured to be 2800 cm^{-3}. The peak volume density, assuming a total path

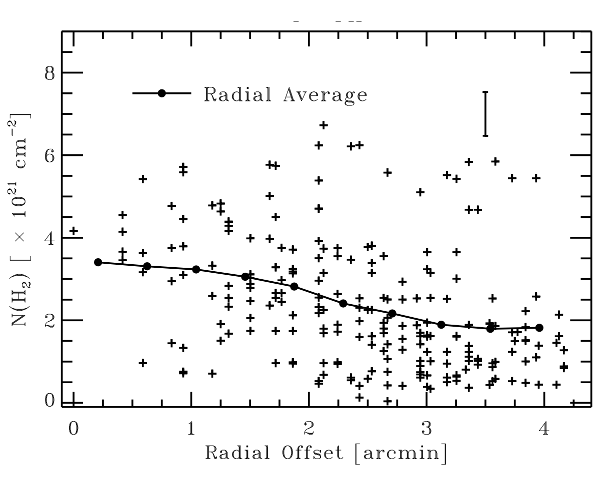

FIG. 7.—GF 9–Fila radial hydrogen column density profile centered at $\Delta\alpha = 0'$, $\Delta\delta = 0'$. The circles connected by the solid line represent a bin-averaged profile (bin size = 25″). A typical 1 σ error bar is shown near the top of the plot.

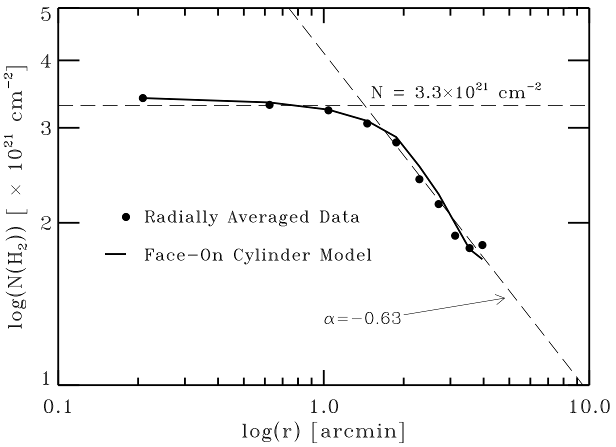

FIG. 8.—GF 9–Fila radially averaged binned H_2 column density data points from Fig. 7 (*filled circles*). The solid line represents the column density profile expected for a face-on uniform-density cylindrical cloud (see text for details). The horizontal dashed line represents the plateau level of $N = 3.3 \times 10^{21}$ cm^{-2} ($r \lesssim 1'$). The sloped dashed line represents the best-fit power law to the model ($\alpha = -0.63$; $r \gtrsim 1'$).

length of 0.56 pc (2 × FWHM), is only ∼1.7 times higher than the mean cloud volume density. The mass and density properties of GF 9–Fila (as a whole) and of the central region are compared in Table 4. These results are consistent with a relatively uniform dust distribution within GF 9–Fila. It should be noted that the same model was applied to GF 9–Core, but a proper fit could not be made, indicating that the high-extinction region in GF 9–Core is not simply a geometric effect.

4. CONCLUSIONS

The filamentary dark cloud GF 9 has been imaged in the near-infrared broadband *J*, *H*, and *K* filters. The observed 7′ × 7′ regions (GF 9–Core and GF 9–Fila) were searched for Class I and Class II young stellar objects. In addition, the line-of-sight near-infrared dust extinction was measured, from which H_2 column density maps were generated. From the column density maps, the mass and density structure of GF 9–Core and GF 9–Fila were determined. The results are summarized below.

1. No Class I or Class II YSOs were detected in either GF 9–Core or GF 9–Fila to within the completeness limits of the photometric data ($J = 16.5$ mag, $H = 15.5$ mag, $K = 15.4$ mag).
2. In particular, no near-infrared counterpart of a Class I or Class II YSO appears to be associated with the *IRAS* point source PSC 20503+6006.
3. Extinction maps were generated from the $E(H-K)$ of background stars. Analysis of the data suggests that the peak extinction toward GF 9–Fila is $A_V \sim 7$ mag. GF 9–Core was *not* fully sampled for extinction to within the photometric completeness limit of the data. In particular, the GF 9–Core high-extinction region ($A_V \gtrsim 10$ mag) was found to be opaque to the limits of the observations.
4. Using the standard gas-to-dust ratio, the extinction maps were converted to H_2 column density maps and were integrated assuming a distance of 440 pc, yielding a mass of 26 $M_\odot$ for GF 9–Core and 22 $M_\odot$ for GF 9–Fila. The average volume density was found to ∼2500 cm^{-3} for both GF 9–Core and GF 9–Fila.
5. The total mass of the region surrounding the *IRAS* point source in GF 9–Core ($r \lesssim 1\overset{'}{.}3$) is ∼9 $M_\odot$, which is ∼35% of the total mass traced by the dust extinction. The mean volume density of the extinction core within GF 9–Core was found to be ∼8000 cm^{-3} with a volume density power-law index of $\gamma \sim -1.6$, a value indistinguishable from the free-fall value ($\gamma = -1.5$).
6. GF 9–Fila displays no strong extinction core. Instead, the dust distribution was found to be consistent with a face-on uniform-density cylindrical cloud.

In summary, we have found that core and diffuse filament regions within FDCs appear to contain similar amounts of mass, yet, only the core region contains a centrally condensed dust core. In contrast, the filamentary region appears clumpy but is relatively consistent with a uniform distribution of dust. As the masses within the two regions are similar, the likely difference between the two regions is the presence of a support mechanism in GF 9–Fila that is no longer present in GF 9–Core. A likely candidate for the support mechanism is a magnetic field. Far-infrared and submillimeter polarimetry would be extremely valuable in testing this hypothesis. In addition, infrared spectroscopy of the reddest sources in GF 9 would allow confirmation of the status of these sources. The near-infrared study of GF 9 has shown that the core and filament regions within FDCs may be fundamentally different from each other and, thus, may provide critical answers to questions regarding the evolution of pre–protostellar and protostellar cores.

This work has been supported, in part, by the Wyoming Space Grant Consortium under NASA grant NGT-40050, by the NSF under grant AST 94-53354, by NASA under grants NAG 5-3395 and NAG 5-3337, by the Aerospace Sponsored Research Program, and by the Office of Research at the University of Wyoming.

REFERENCES

Barsony, M. 1994, in ASP Conf. Ser. 65, Clouds, Cores, and Low-Mass Stars, ed. D. P. Clemens & R. Barvainis (San Francisco: ASP), 197
Beichman, C., Myers, P. C., Emerson, J. P., Harris, S., Mathieu, R., Benson, P. J., & Jennings, R. E. 1986, ApJ, 307, 337
Benson, P. J., & Myers, P. C. 1989, ApJS, 71, 89
Bessel, M. S., & Brett, J. M. 1988, PASP, 100, 1134
Bohlin, R. C., Savage, B. D., & Drake, J. F. 1978, ApJ, 224, 132
Bok, B. J. 1937, The Distribution of the Stars in Space (Chicago: Univ. Chicago Press)
Bontemps, S., Andrè, P., Terebey, S., & Cabrit, S. 1996, A&A, 311, 858
Cardelli, J. A., Clayton, G. C., & Mathis, J. S. 1989, ApJ, 224, 132
Chandrasekhar, S., & Fermi, E. 1953, ApJ, 118, 116
Ciardi, D. R. 1997, Ph.D. thesis, Univ. Wyoming
Ciardi, D. R., Woodward, C. E., Clemens, D. P., Harlzer, D. E., & Rudy, R. J. 1998, in preparation
Dickman, R. L., & Herbst, W. 1990, ApJ, 357, 531
Dobashi, K., Bernard, J., Yonekura, Y., & Fukui, Y. 1994, ApJS, 95, 419
Elias, J. H., Frogel, J. A., Matthews, K., & Neugebauer, G. 1982, AJ, 87, 1029
Frerking, M. A., Langer, W. D., & Wilson, R. W. 1982, ApJ, 262, 590
Garwood, R., & Jones, T. J. 1987, PASP, 99, 453
Goodman, A. A., Benson, P. J., Fuller, G. A., & Myers, P. C. 1993, ApJ, 406, 528
Greenstein, J. L. 1951, in Astrophysics, ed. J. A. Hynek (New York: McGraw Hill), chap. 13
Howell, S. B. 1989, PASP, 101, 616
IRAS Catalogs and Atlases: Explanatory Supplement. 1988, ed. C. A. Beichman, G. Neugebauer, H. J. Habing, P. E. Clegg, & T. J. Chester (Washington: GPO)
Jenkins, E. B., & Savage, D. B. 1974, ApJ, 187, 243
Kane, B. D. 1995, Ph.D. thesis, Boston Univ.
Lada, C. J., & Adams, F. C. 1992, ApJ, 393, 278

Lada, C. J., Lada, E. A., Clemens, D. P., & Bally, J. 1994, ApJ, 429, 694

Lilley, A. E. 1955, ApJ, 121, 559

Mathis, J. S. 1990, ARA&A, 28, 37

McCutcheon, W. H., Vrba, F. J., Dickman, R. L., & Clemens, D. P. 1986, ApJ, 309, 619

Myers, P. C., & Benson, P. J. 1983, ApJ, 266, 309

Myers, P. C., Linke, R. A., & Benson, P. J. 1983, ApJ, 264, 517

Rieke, G. H., & Lebofsky, M. J. 1985, ApJ, 288, 618

Rudy, R. J., Rossano, G. S., & Puetter, R. C. 1996, ApJ, 458, L41

Saraceno, P., André, P., Ceccarelli, C., Griffin, M., & Molinari, S. 1996, A&A, 309, 827

Schneider, S., & Elmegreen, B. G. 1979, ApJS, 41, 87

Shu, F. H. 1977, ApJ, 45, 121

Shu, F. H., Adams, F. C., & Lizano, S. 1987, ARA&A, 25, 23

Stetson, P. B. 1987, PASP, 99, 191

Straw, S. M., & Hyland, A. R. 1989, ApJ, 340, 318

Terebey, S., Vogel, S. N., & Myers, P. C. 1989, ApJ, 340, 472

Vrba, F. J., & Rydgren, A. E. 1985, AJ, 90, 1490

Wainscoat, R. J., & Cowie, L. L. 1992, AJ, 103, 332

Wu, Y., Zhou, S., & Evans, N. J., II. 1992, ApJ, 394, 196

Yang, J., Umemoto, T., Takahiro, I., & Fukui, Y. 1991, ApJ, 373, 137

Yun, J. L., & Clemens, D. P. 1990, ApJ, 367, L73

———. 1991, ApJ, 381, 474

———. 1995, AJ, 109, 742